Physics-informed stereology for estimating placental diffusive exchange capacity

Richard Mcnair[a], Carl Whitfield[b], Gowsihan Poologasundarampillai[c], Oliver E. Jensen[b], Igor L. Chernyavsky[b,d,*]

[a]*Department of Mechanical, Materials and Manufacturing Engineering, University of Nottingham, University Park, Nottingham, NG7 2RD, UK*
[b]*Department of Mathematics, University of Manchester, Oxford Road, Manchester, M13 9PL, UK*
[c]*Faculty of Dentistry, Oral and Craniofacial Sciences, King's College London, Great Maze Pond, London, SE1 1UL, UK*
[d]*Maternal and Fetal Health Research Centre, University of Manchester, Oxford Road, Manchester, M13 9WL, UK*

Abstract

Introduction: Stereological estimates of villous membrane thickness and surface area are widely used to infer the diffusive exchange capacity of the human placenta. A key geometric determinant of exchange capacity can be expressed as an effective diffusive length scale. Here we combine virtual histological sections with computational modelling in realistic villous geometries to assess the accuracy of classical stereological estimates of this diffusive length scale.
Methods: Two terminal villi, reconstructed from three-dimensional imaging, were digitally sectioned to generate random two-dimensional geometries containing fetal capillaries and surrounding villous tissue. For each section, we simulated steady diffusive transport between the fetal capillary and intervillous space boundaries to obtain a physics-based diffusive length scale as a reference case. Using the same geometries, we applied standard line–intercept stereology to measure harmonic-mean barrier thickness and boundary–length densities, from which a stereological estimate of diffusive length scale was derived.
Results: Across both villi, stereology systematically overestimated the diffusive length scale by approximately 15–25%, depending on villus and section. We identified sources of this discrepancy, including interface curvature and assumptions underpinning the stereological correction factors, using idealised models of villus structure.

*Corresponding author: igor.chernyavsky@manchester.ac.uk

Conclusion: These findings highlight the need for stereological approaches that account for curvature when interpreting placental structure–function relationships.

Keywords: human placenta, stereology, 3D imaging, mathematical modelling, diffusive transport

---

1. Introduction

In the human placenta, maternal blood flows from spiral arteries into a cavity filled with a villous tree of vascularised fetal tissue. The flow around this tree transports nutrients, which diffuse across a thin tissue barrier into the fetal circulation, with waste products diffusing the other way (Baergen et al., 2022). The thickness of this barrier, and its spatial variation, are key determinants of the diffusive capacity of the placenta in health and disease (Barapatre et al., 2026; Sun et al., 2020; Bappoo et al., 2024).

Many important species, such as oxygen, passively diffuse across the barrier (Nye et al., 2018; Gill et al., 2011). This process can be modelled using standard diffusion equations involving diffusion coefficients of the various species in human tissue (Perazzolo et al., 2017). The diffusive capacity of a barrier is directly proportional to a diffusive length scale $\mathcal{L}$ (Erlich et al., 2019; Jensen and Chernyavsky, 2019). The diffusive exchange capacity is defined as the total diffusive transfer rate J_d across the exchange barrier driven by a fixed concentration difference Δc, which can be written in the form

$$J_d = D\,\Delta c\,\mathcal{L}, \tag{1.1}$$

where D is the diffusion coefficient in tissue. Thus, $\mathcal{L}$ summarises the morphometric component of diffusive exchange capacity, integrating both barrier thickness and its spatial variation. Historically (Mayhew et al., 1984, 2007), and in recent studies (Yong et al., 2023), $\mathcal{L}$ has been approximated as the mean total exchange surface area divided by the harmonic mean of the barrier thickness, both of which can be estimated using stereological methods (Weibel and Knight, 1964).

Stereology is the technique for deriving information about higher dimensional structures from lower-dimensional data. In the present context, this is usually investigated by fixing donated placental tissue in some substance such as wax, and then cutting the tissue randomly to reveal two-dimensional

geometries on the faces of the cuts (Jackson et al., 1985). For calculating barrier thickness, stereologists overlay a grid of randomly-oriented lines onto the two-dimensional image (a cut piece of placental tissue), and then relate the intercept length of these random lines with the barrier to the harmonic thickness by stereological formulae (Mayhew, 2006; Feneley and Burton, 1991). For calculating surface area or perimeter length (in 3D or 2D respectively), the intercept count of random lines per unit length of line can be related to the surface-area or perimeter density. These formulae are derived by calculating an expected value for the length of intersection/intercept count per unit length of a random line given the true thickness (Jensen et al., 1979; Gundersen et al., 1978). Many approximations are made in both the definition of the true thickness used in the derivation of the formulae, and in the calculation of this expected value (Mayhew, 2006).

This traditional stereological approach was developed when only limited tissue sampling and imaging resolution were available, and it relies on geometric idealisations of the barrier that may not hold in the highly curved architecture of terminal villi. Today, high-resolution three-dimensional imaging and computational modelling (Chappell et al., 2023; Lewis and Pearson-Farr, 2020) allow us to evaluate how well classical stereological estimators recover diffusion-relevant quantities when applied to realistic villous geometries. This creates an opportunity to quantify possible systematic geometric bias, which is important when stereology-derived thicknesses and surface areas are propagated into estimates of placental diffusive capacity.

In this study, we use recent imaging data from micro-computed tomography (μCT) and confocal laser-scanning microscopy (CLSM) derived datasets to sample randomised 2D geometries from villi by slicing the geometry into randomised sections and calculating $\mathcal{L}_p$, the two-dimensional analogue of $\mathcal{L}$, to quantify diffusive exchange capacity on each slice. Formal definitions of $\mathcal{L}$ and $\mathcal{L}_p$ are given in Appendix A. We compare these "physics-based" reference values to stereology-based estimates derived using established stereological approaches.

This study makes three contributions that directly inform interpretation of placental morphometric diffusion metrics. First, the physics-based values of $\mathcal{L}_p$ provide new data to inform unbiased estimates of terminal villus diffusive capacity. Second, we quantify systematic error in stereological estimates and the uncertainty due to sampling. Third, we identify the geometric features of villous architecture, particularly curvature of thin exchange regions, that are the source of bias in stereological estimates of barrier thickness and

diffusive length scale.

Throughout this work, we distinguish three different sources of error in stereological estimation of diffusive length scales or "exchange capacity". The first is *stereology-formula* error, which is the bias introduced due to the assumption of an unbounded planar barrier made in the derivation of stereological formulae linking harmonic-mean random intercept length with harmonic-mean barrier thickness. The second is *model-reduction* error, which is the discrepancy introduced when the diffusive length scale is approximated from the geometric proxy of an average perimeter or surface-area divided by a harmonic-mean barrier thickness. The third is *image-segmentation* error. The translation from raw images to labelled datasets inevitably involves errors and can produce significant artefacts, especially when quantifying surface areas and the thickness of thin barriers.

The layout of this paper is as follows. In Section 2 we detail our method for directly calculating surface area and diffusive length scale from two terminal villus geometries. We then detail our methods for randomly sampling 2D sliced geometries from the villi, and explain how we replicate stereological methods for calculating surface areas and harmonic mean thicknesses. We apply these methods to some simplified geometries where the thickness and diffusive capacity are known. In Section 3 we compare the stereologically-approximated surface areas and diffusive length scales with reference (physics-based) values. In Section 4, we discuss a possible source for the observed discrepancies in terms of surface curvature.

2. Model and methods

Table 1 defines all of the symbols used in the main text to represent measured quantities and model parameters. Table 2 provides a brief summary of the sample preparation and imaging protocols alongside the 3D morphological analysis of the two villous specimens (see Fig. 1).

2.1. Approximation of stereological techniques on computational data

We performed stereological experiments on two terminal villus geometries (Fig. 1), which we identify as villus 1 and villus 2. Each villus was imported into `COMSOL Multiphysics 6.3`® (COMSOL AB, 2024) and enclosed within a rectangular bounding box (Fig. 2a,b) which is needed to calculate perimeters from stereologically obtained perimeter densities. Two-dimensional slices were generated by intersecting the villus and its bounding

Symbol	Description	Units
	Reported measures	
$\mathcal{L}$	Reference (physics-based) diffusive length scale of entire villus.	μm
$\mathcal{L}_p$	Reference (physics-based) diffusive length scale per unit depth of a sampled 2D slice, defined in equation (A.3).	–
$\widehat{\mathcal{L}}_p$	Stereologically-estimated diffusive length scale per unit depth of a sampled 2D slice, defined in equation (2.3).	–
P_t, P_v	Reference total perimeter of tissue (villus-IVS interface) and capillary (villus-capillary interface) respectively in a sampled 2D slice.	μm
$\widehat{P}_t$, $\widehat{P}_v$	Stereologically-estimated total perimeter of tissue and capillary respectively, in a sampled 2D slice.	μm
h	Reference (physics-based) effective barrier thickness in a 2D slice, calculated as mean reference perimeter divided by $\mathcal{L}_p$.	μm
$\widehat{h}$	Stereologically-estimated effective barrier thickness in a 2D slice, calculated by equation (2.2).	μm
	Stereology parameters	
A_{ROI}	Area of region of interest (ROI)	μm^2
N	Number of random lines generated in ROI	–
I_t, I_v	Number of intercepts of generated lines with tissue and capillary surfaces respectively, for a given set of lines and 2D slice.	–
T_i	Length of a line section that passes from the inner to outer villus interface, for a given line and 2D slice.	μm
	Idealised model parameters	
κ	Curvature of the circular interface used in Section 3.1.	μm^{-1}
d	Thickness of the planar-band and annular benchmark geometries used in Section 3.1.	μm

Table 1: Symbols used in this study to represent various quantities, either defined as model outputs or measured as input parameters.

	Specimen 1	Specimen 2
Modality	Synchrotron μCT	Confocal microscopy
Sample/Data ID	123761	1
Clinical characteristics	Term CS; healthy pregnancy	Term CS; healthy pregnancy
Fixation and embedding	Z7+PFA perfusion fixed; Batson's infiltrated via fetal side; critical point dried	Perfusion-fixed with formalin
Staining	–	FITC-conjugated Ulex lectin (perfused; vessels); DiI dye (immersed; syncytium)
Feature extraction software	Avizo	3DSlicer; SolidWorks
Raw imaged volume (μm^3)	$\lesssim 10^{10}$	$\sim 10^7$
Voxel size: x, y, z (μm)	0.81, 0.81, 0.81 [a]	0.28, 0.28, 2.00 [b]
Total specimen volume (μm^3)	1.96×10^5	2.59×10^6 [b]
Capillary volume fraction	0.34	0.28 [b]
Capillary-to-villous surface ratio	1.01	1.05 [b]
Harmonic mean thickness (μm)	–	8.37 [c]
Directly calculated diffusive length-scale $\mathcal{L}$ (μm)	0.62×10^4	0.79×10^4

Table 2: Summary of imaging, sample preparation, and morphometric characteristics for the two terminal villus datasets analysed (Specimen 1: synchrotron μCT; Specimen 2: confocal microscopy). Sources: [a] Tun et al. (2021); [b] Plitman Mayo et al. (2016); [c] Plitman Mayo et al. (2019), Erlich et al. (2019).

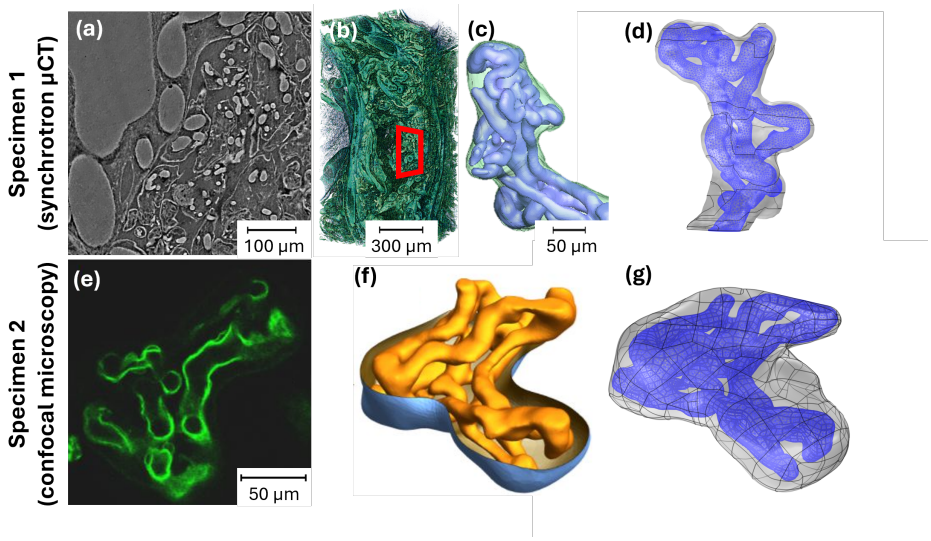

Figure 1: Creation of terminal villus datasets and computational meshes used for slicing and stereological analysis. (a–d) Villus 1 from synchrotron μCT (Tun et al., 2021). (a) A representative 2D slice showing villi and vessels. (b) 3D rendering of a smaller region of interest showing the complex placental architecture. (c) 3D rendering of a terminal villus and capillaries. (d) Finite-element mesh of the terminal villus geometry imported into COMSOL Multiphysics. (e–g) Villus 2 from confocal microscopy. (e) 2D confocal slice of the villus. (f) Segmented surface geometry of the villus and capillary network. (g) Corresponding finite-element mesh in COMSOL used for random slicing and stereological analysis.

box with uniformly-randomly oriented planes, producing, for each villous specimen, a set of 20 2D slice geometries (Fig. 2c). Slices were retained only if the plane intersected both the tissue and capillary domains and for villus 2, slices intersecting a cropped edge were excluded. This yielded 15 valid slices for villus 1 and 8 for villus 2. Each slice contains (i) the tissue boundary, (ii) the capillary boundary, and (iii) the bounding polygon that defines the region of interest (ROI). All implementation details required for reproducibility of the methods are provided in Appendix C. We perform the analysis here in two dimensions only, as it allows more data to be generated for comparison. The corresponding three-dimensional estimators are obtained by pooling intercept counts and intercept lengths over multiple sections, and differ only by standard numerical conversion factors (Gundersen et al., 1978). Thus, the stereology-formula and model-reduction type errors we find in two dimensions are expected to persist to the 3D case too.

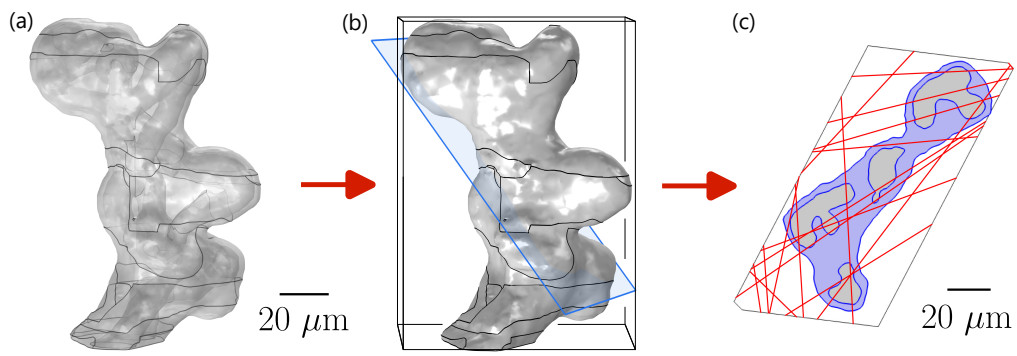

Figure 2: Overview of the stereological workflow. (a) Villus 1 geometry is imported into COMSOL. (b) A rectangular bounding box is drawn around the villus, and a random slice is sampled through the villus and box. (c) The work plane yields a 2D slice geometry consisting of the villus outline, capillary outline, and a bounding polygon defining the region of interest (ROI). Random test lines are overlaid on the slice and used to estimate perimeter lengths and harmonic-mean barrier thickness.

For each slice, COMSOL was used to compute reference values against which stereological estimates were compared. These included the total tissue and capillary perimeters, P_t and P_v respectively, measured directly from the slice geometry, and the 2D diffusive length scale $\mathcal{L}_p$ obtained by solving the steady diffusion equation on the same slice.

To present diffusion-based predictions in a form that is directly comparable to classical harmonic-mean thickness measurements, we define a reference effective thickness, h, for each two-dimensional slice. This is the thickness of a notional uniform planar barrier that would give the same overall diffusive exchange as the original slice geometry under the same concentration difference.

For each slice, a high-resolution image was exported together with its spatial dimensions. Each image was segmented into tissue, capillary, and intervillous space (IVS) within the ROI. Stereological estimators were then applied to each segmented slice using random test lines overlaid within the ROI, as illustrated in Figure 2(c).

2.1.1. Total perimeter and harmonic mean barrier thickness estimation from random lines

Perimeters were estimated from the number of boundary crossings made by 500 isotropic uniform random test lines overlaid onto each segmented slice

image. Let I_t and I_v denote the total number of intercepts between the test lines and the tissue–IVS boundary and the tissue–capillary boundary respectively. Let L_T denote the total length of all test-line segments lying within the ROI, and let A_{ROI} denote the ROI area in the slice. The stereological estimates of the tissue and capillary perimeters on a slice are (Romppanen and Collan, 1983; Cruz-Orive, 2017)

$$\widehat{P}_i \;=\; A_{\mathrm{ROI}}\,\frac{\pi}{2}\,\frac{I_i}{L_T}, \qquad i = t, v. \tag{2.1}$$

This is the standard isotropic uniform random line-intercept estimator for boundary length density in 2D. $\widehat{P}_t$ and $\widehat{P}_v$ seek to estimate P_t and P_v respectively.

Barrier thickness was estimated from tissue chord lengths sampled along the random test lines. Each chord corresponds to a portion of a test line passing through tissue between IVS and capillary. The slice-level stereological estimate of harmonic-mean barrier thickness is derived in Appendix B as

$$\widehat{h} \;=\; \frac{\pi}{4}\left(\frac{N}{\sum_{i=1}^{N}\frac{1}{T_i}}\right), \tag{2.2}$$

where T_i denotes intercept length of a random line and N is the number of random lines generated (the 3D relation can be found in standard references like Jensen et al. (1979)).

2.2. Stereological proxy for the diffusive length scale

From the stereological measures above, we define a slice-level estimate of the diffusive length scale per unit depth by combining perimeter and thickness estimates as

$$\widehat{\mathcal{L}}_p \;=\; \frac{\widehat{P}_t + \widehat{P}_v}{2\,\widehat{h}}. \tag{2.3}$$

This proxy uses the arithmetic mean of the tissue and capillary perimeters, normalised by the harmonic-mean barrier thickness, which is the typical approximation used in literature (Mayhew et al., 1984, 2007; Yong et al., 2023). The resulting $\widehat{\mathcal{L}}_p$ values were compared directly against the reference $\mathcal{L}_p$ values computed in COMSOL on the same slices.

Sampling uncertainty due to the finite number of random test lines was quantified using bootstrap resampling at the level of test lines within each

slice. For each slice, repeated resampling with replacement produced empirical distributions for the estimated perimeters $\widehat{P}_t$, $\widehat{P}_v$, harmonic mean thickness $\widehat{h}$, and diffusive length scale per unit depth $\widehat{\mathcal{L}}_p$, from which 95% confidence intervals were reported. Full details of the bootstrap procedure are given in Appendix C.

3. Results

3.1. Experiments on simplified geometries

To help interpret errors for predicting barrier thickness from stereological methods, we carried out two benchmark experiments using simplified synthetic images where the barrier thickness is known exactly. In both experiments, we generated labelled 2D images representing a tissue barrier separating a vessel region from the intervillous space, and then applied the random-line stereological thickness pipeline used in the main slice experiments. Repeating the experiment many times allowed us to separate any bias from random variation caused by finite sampling. These experiments reveal errors of stereology-formula type only and thus help us understand the relative contribution of both stereology-formula and model-reduction errors in our experiments on the villus geometries.

First, we tested a planar barrier of constant thickness spanning the full width of the image (Fig. 3a). This geometry is designed to isolate the effect of finite barrier aspect ratio: when the barrier is not very thin compared with the overall field of view, stereological assumptions become less accurate. We repeated the experiment across a range of barrier thicknesses while adjusting the image resolution so that the barrier was always similarly well-resolved in pixels (Appendix C, Fig. C.1). This allowed us to attribute any remaining error to geometry rather than pixellation.

Second, we tested a curved barrier formed by two concentric circles, giving a tissue annulus of constant thickness but with varying curvature (Fig. 3b). By changing the circle radius while keeping the barrier thickness fixed, we generated barriers that ranged from weakly to strongly curved. This geometry isolates curvature-driven bias in harmonic-mean thickness estimation. As with the planar experiment, results were obtained by repeated random-line sampling, and the mean error was summarised across trials to identify how bias depends on curvature.

The model-reduction errors in these geometries for $\mathcal{L}_p$ and $\mathcal{L}$ (reported in Appendix D) are proportional to the dimensionless parameter $d\kappa$, where

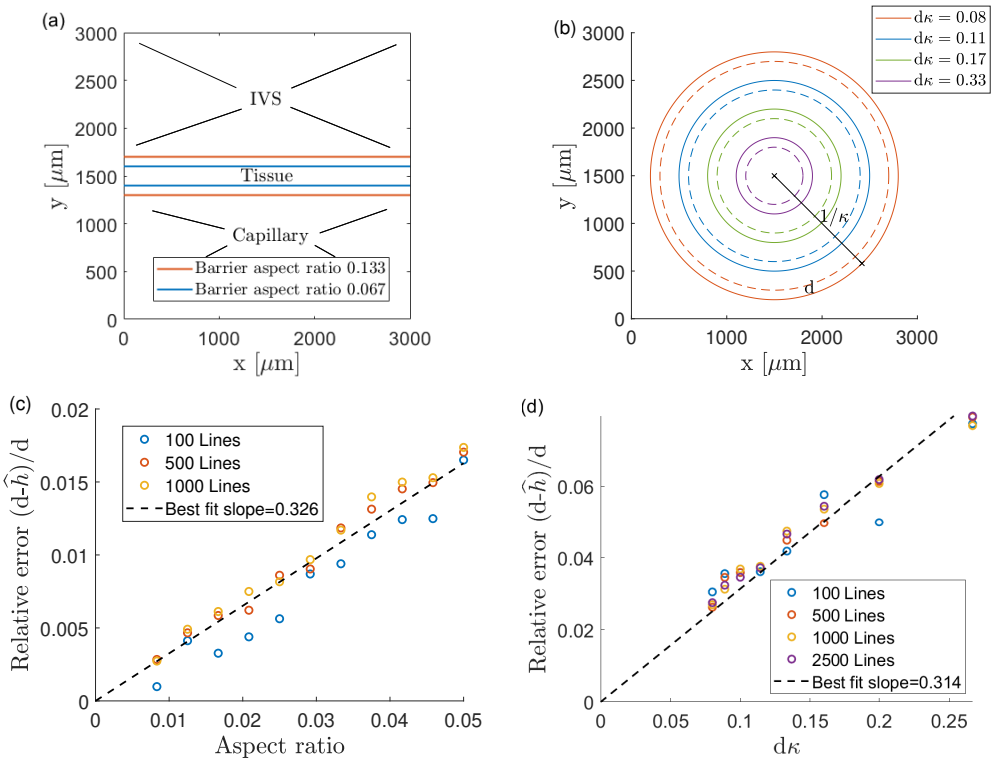

Figure 3: Experiments on simplified geometries. (a) Schematic of a finite-aspect-ratio barrier. Blue lines show a barrier of aspect ratio 0.067, red curves show a barrier with aspect ratio 0.133. (b) Schematic of the annular geometries considered. Solid curves denote the outer boundary and dashed curves the inner boundary. Colours indicate different radii $1/\kappa$ (equal to the inverse of curvature κ); the barrier thickness is a constant d across geometries. (c) Relative error in stereological approximations h of barrier thickness d versus barrier aspect ratio for the planar barrier geometries in experiments using 100, 500 and 1000 lines, showing convergence as the aspect ratio tends to zero. Best fit slope shows approximate error as 0.326 times the aspect ratio. (d) Relative error in stereologically approximated thickness for the annular geometries against non-dimensional parameter dκ. A best-fit slope quantifies error as approximately 0.314 dκ.

d is the barrier thickness and κ is the interface curvature. We consider the stereology-formula errors also in terms of $d\kappa$ to directly compare their relative contributions.

Figure 3 reports the benchmark experiments on the simplified geometries designed to isolate expected sources of bias. The planar experiment (Fig. 3c) demonstrates convergence of the stereological harmonic-mean thickness estimate as the barrier aspect ratio decreases, consistent with the locally planar assumptions underlying the correction factors. The concentric annulus experiment (Fig. 3d) shows an approximately linear increase in the relative thickness error with the dimensionless curvature parameter $d\kappa$, supporting the interpretation that curvature-driven deviations from the locally-flat idealisation systematically underestimate thickness and hence overestimate $\mathcal{L}_p$. Across Figures 3 and 4, bootstrap confidence intervals quantify sampling variability arising from the finite number of random test lines, while the fitted slopes highlight systematic disagreement that persists beyond this sampling uncertainty.

3.2. Experiments on villus geometries

Figure 4 summarises the slice-by-slice stereological estimates compared with reference values computed directly from the COMSOL geometries. In Figure 4(a), stereological perimeter estimates show a small but consistent bias. Linear fits through the origin for the four data series (tissue and vessel perimeters in villi 1 and 2) have slopes 0.941, 0.922, 0.941 and 0.961, respectively, indicating that the computational procedure systematically biases the stereologically-estimated perimeters to be slightly larger than their reference values. A plausible source of this discrepancy is segmentation-induced jaggedness of the tissue and vessel boundaries, which increases the measured interface length relative to the underlying smooth geometry. Importantly, the magnitude of this perimeter bias is modest compared with the thickness bias described below.

In contrast, Figure 4(b) shows a larger systematic discrepancy in barrier thickness compared with the "physics-based" thickness (that is, the uniform effective thickness that reproduces the same diffusion-derived exchange capacity as the original slice geometry). The stereological harmonic-mean thickness is biased low compared with the physics-based estimates, with best-fit slopes of 1.150 for villus 1 and 1.132 for villus 2 (i.e. the reference thickness is $\approx$ 13–15% larger than the stereological estimate across slices). This indicates that classical line-intercept stereology, when applied to these

realistic villus sections, tends to underestimate the effective exchange-barrier thickness. Since the diffusive length-scale proxy $\widehat{\mathcal{L}}_p$ depends inversely on thickness, this systematic thickness bias dominates the overall behaviour of the stereological estimate $\widehat{\mathcal{L}}_p$.

Figure 4(c) shows that stereology systematically overestimates $\mathcal{L}_p$, with best-fit slopes (for physics-based versus stereological estimate) of 0.798 and 0.853 for villi 1 and 2, respectively. Equivalently, the stereological estimate is typically larger than the reference value by approximately 15–25%. Figure 4(d) highlights the highly curved, thin regions that contribute strongly to the harmonic-mean thickness. The thinnest regions in representative slices correspond to typical values of $d\kappa \approx 0.23$–0.31, which is an important quantity we discuss next.

4. Discussion

4.1. Principal findings

In this study, we used fully segmented 3D villous geometries and numerical solutions of the diffusion equation to quantify the accuracy of classical stereological methods for estimating placental exchange barrier thickness and diffusive exchange capacity. By comparing stereological estimates obtained from virtual 2D sections with reference values derived from computational solutions, we showed that conventional line-intercept–based stereology systematically overestimates the diffusive length-scale $\mathcal{L}_p$ in 2D images. By extension, the overall villus diffusive length scale $\mathcal{L}$ will also be overestimated. This bias was observed in two independent villous geometries obtained from distinct imaging modalities and segmentation pipelines, suggesting that it reflects generic geometric features of villous architecture rather than idiosyncrasies of a single specimen or modality.

Our analysis further indicates that this bias is strongly linked to local curvature of the fetal capillary–syncytiotrophoblast interface. The discrepancy arises from two distinct sources. First, there is stereology-formula error. Even with exhaustive *in silico* sampling, the classical line-intercept correction factors are derived under idealised assumptions of locally planar, parallel interfaces, so they do not fully account for curvature-dependent terms. Second, there is model-reduction error. Approximating diffusive capacity using the ratio of mean surface area to harmonic-mean thickness is itself a geometric simplification, and becomes increasingly inaccurate when barrier thickness

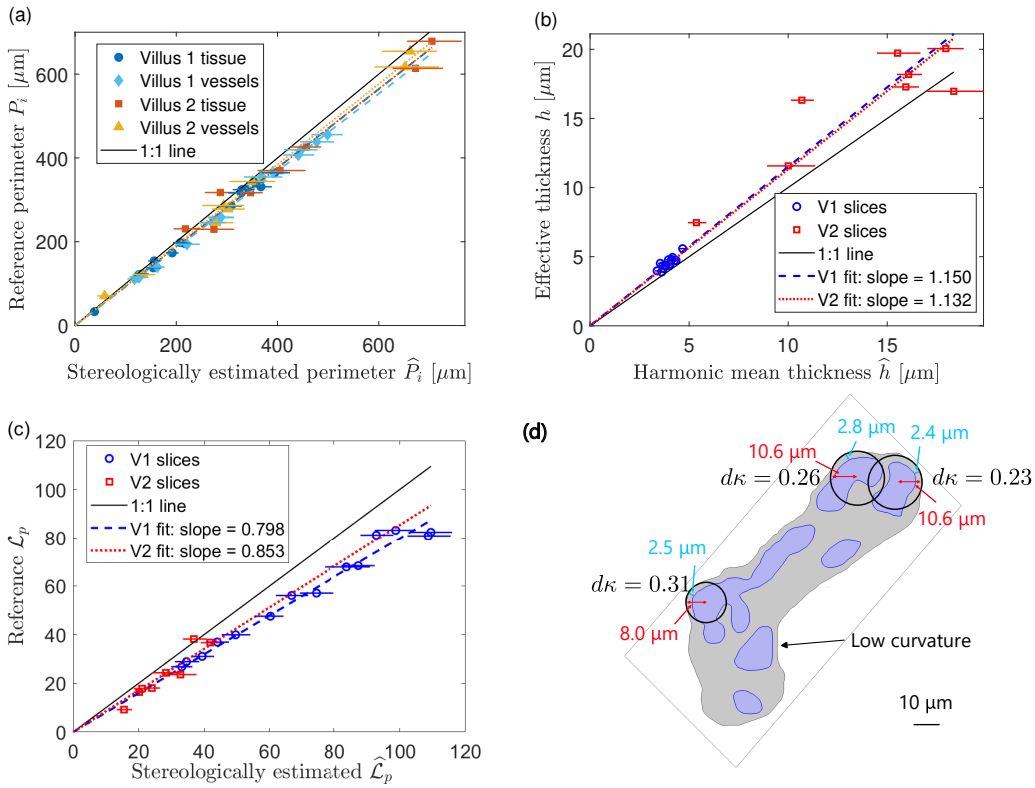

Figure 4: Results from the stereological experiments using images of villi. (a) Stereologically-estimated perimeter (x-axis) is plotted against the reference perimeter (y-axis). Best-fit dashed lines of slope 0.941, 0.922, 0.941 and 0.961 for villus 1 tissue, villus 1 vessel, villus 2 tissue and villus 2 vessel respectively compare the estimated and reference values. (b) The stereologically estimated harmonic-mean thickness (x-axis) is compared with the physics-based thickness (y-axis). (c) The stereology-based estimate $\widehat{\mathcal{L}}_p$ (x-axis), defined by equation (2.3) is compared with the reference diffusive length scale $\mathcal{L}_p$ (y-axis). In (a)–(c), error bars show 95% bootstrap confidence intervals for the stereological estimates, and best-fit lines are included to highlight systematic disagreement. (d) A representative slice with circles marking the thinnest regions of the tissue boundary, illustrating typical local curvatures and demonstrating consistency with the curvature-based error approximation in (D.3) of Appendix D.

varies over a curved interface. Consequently, stereological estimates of thickness and surface–area–to–volume ratios may not converge to the numerically derived values for $\mathcal{L}$ even as sampling density increases. Together, these findings suggest that while stereology provides useful relative comparisons between groups, its use to infer absolute diffusive capacity requires careful re-evaluation when curvature and thickness heterogeneity are substantial.

4.2. Comparison with previous work

Stereological methods have been central to quantitative placental morphometry for several decades, underpinning much of our understanding of how villous structure supports feto-placental exchange. Numerous studies (Mayhew et al. (1984, 2007); Yong et al. (2023) etc.) used point-counting and line-intercept techniques to estimate villous volume, capillary surface area, and thickness of the villous membrane, and then combined these measures into morphometric indices of diffusive capacity. In particular, the concept of a harmonic-mean barrier thickness, often estimated from line-intercept distributions, has been widely used as a surrogate for the effective path length for diffusion.

By explicitly solving the diffusion problem in realistic geometries, we show that the effective diffusive length depends not only on harmonic-mean barrier thickness and surface area, but also on how that thickness and area are distributed in space and curved in relation to the driving concentration gradient. Classical stereological formulae effectively collapse these details into a planar approximation, which is violated in villi with tortuous capillaries, bulging syncytial knots, and irregular microvillus patterns.

The overestimation of $\mathcal{L}_p$ that we observe is therefore consistent with the idea that stereological estimates of harmonic-mean thickness, derived from line intercepts across complex curved interfaces, do not fully capture the impact of geometry on diffusive pathways. Our curvature-based analysis suggests that systematic deviations from planarity accumulate into appreciable biases when propagated through the standard formulae linking thickness, surface area, and diffusive capacity.

4.3. Methodological implications for placental stereology

The most immediate implication of this work is methodological. Our results do *not* imply that stereology is invalid for studying placental structure, but they do highlight the following points.

1. Absolute values of diffusive exchange capacity derived from classical formulae should be interpreted with caution. In practical terms, the magnitude of bias we observe is not negligible if stereology underestimates barrier thickness and overestimates $\mathcal{L}_p$ by approximately 15–25% (Fig. 4c); this directly impacts absolute barrier-thickness values (Feneley and Burton, 1991; Ong and Burton, 1991). Since morphometric formulations show diffusive capacity as proportional to the diffusion coefficient multiplied by an effective diffusive length scale, this implies that stereology-based capacity estimates could be inflated by a comparable percentage, even before considering additional experimental sources of error. This matters because changes of similar magnitude are frequently discussed in the literature as evidence of functional impairment or adaptation.
2. Relative comparisons are likely more robust than absolute values. Despite the bias, we found reasonably consistent relationships between stereological and numerical estimates across slices, indicating that stereology captures differences in barrier thickness and surface–area–to–volume ratios between regions or groups, provided sampling and analysis are identical.
3. Correcting for curvature (Appendix D) may improve stereological estimates. Our derivations show that curvature terms naturally enter the expressions linking 2D intercept statistics to 3D effective thickness. Although we have not yet distilled a simple, universally applicable correction factor, the analysis suggests a route towards modified stereological formulae that explicitly incorporate measures of interface curvature or shape.

4.4. Limitations

Several limitations of our study should be acknowledged. First, our analysis is based on only two terminal villi, each reconstructed from a different imaging modality. While these villi are representative in terms of size and complexity, they cannot capture the full variability of villous architecture within and between placentas. Our conclusions about systematic bias should therefore be considered provisional until confirmed across a larger set of geometries spanning different gestational ages and clinical conditions.

Second, the numerical diffusion model is intentionally idealised. We assumed steady-state diffusion of a passive solute with a uniform diffusion coefficient, ignored binding, facilitated transport and consumption, and did

not explicitly model heterogeneity in membrane composition. These simplifications are appropriate for isolating the geometric component of diffusive resistance. However, the derived values of $\mathcal{L}$ should not be interpreted as precise physiological quantities for any given solute.

Third, although we performed stereology on virtual sections to avoid cutting and processing artefacts, the segmentation and sampling protocols still introduce sources of error. Mis-classification at tissue boundaries, partial-volume effects at the voxel level, and choices about line density and step length can all affect estimated perimeter and thickness statistics. In experimental settings, additional biases due to fixation shrinkage, tissue deformation, and incomplete sampling of the villous tree are likely to be present.

Finally, our curvature analysis is currently restricted to relatively simple idealised geometries and local approximations. Extending this to more general surfaces, and developing practical curvature metrics that can be extracted from routine histological sections, remain important tasks for future work.

4.5. Future directions

Building on these findings, some avenues for future research are apparent. First, the stereology–simulation comparison should be extended to a larger cohort of villi and placentas, including both uncomplicated and pathological pregnancies. This would allow the magnitude and direction of stereological bias to be quantified across a wider spectrum of villous morphologies.

Second, it would be valuable to derive and validate simplified correction factors or lookup tables that map commonly measured stereological indices (such as harmonic-mean thickness and surface area) to effective diffusive exchange capacity for typical placental geometries. Such tools could make 3D, curvature-aware corrections accessible to groups without extensive modelling expertise.

4.6. Conclusions

In summary, by combining realistic villous geometries with computer simulations of the diffusive transport process, we have shown that classical stereological methods tend to overestimate the effective diffusive exchange capacity for solute transfer across the placental exchange barrier. This bias arises from assumptions of planarity and the neglect of curvature in the standard stereological formulae, and it persists even when sampling is dense and unbiased in two dimensions. While stereological methods are valuable for

comparative morphometric studies, their use for deriving absolute diffusive exchange capacities should be treated with caution, ideally in conjunction with 3D modelling. Recognising and correcting for these geometric effects will improve the quantitative interpretation of placental structure–function relationships and may sharpen our understanding of how villous remodelling contributes to both normal and pathological feto-placental exchange.

Acknowledgements:

This work was partly supported by the Wellcome Leap *In Utero* programme. We thank Paul Brownbill, Angelos Evangelinos, Simon Cotter and Alexander Heazell (University of Manchester) and Michele Darrow and Avery Pennington (Rosalind Franklin Institute) for helpful discussions.

Appendix A. Definition of the diffusive length scale

The diffusive length scale for a barrier in three-dimensions is defined by

$$\mathcal{L} = \int_S \mathbf{n} \cdot \boldsymbol{\nabla} c \, \mathrm{d}A, \tag{A.1}$$

where S is one of the surfaces enclosing the barrier, and c satisfies

$$\nabla^2 c = 0 \quad \text{in } \Omega, \qquad c = 1 \text{ on } S_1 \quad \text{and} \quad c = 0 \text{ on } S_2. \tag{A.2}$$

Ω is the region of space occupied by the barrier. In two dimensions, the diffusive length scale per unit length is defined as

$$\mathcal{L}_p = \int_P \mathbf{n} \cdot \boldsymbol{\nabla} c \; \mathrm{d}s \tag{A.3}$$

where P is one of the perimeters enclosing the barrier, $\mathrm{d}s$ is an arc-length along the perimeter and c satisfies Laplace's equation on the region in which Ω intersects the plane.

Appendix B. Relating sampled intercept lengths to the true mean thickness

This appendix derives the standard proportionality between the harmonic mean of sampled line intercept lengths and the perpendicular thickness of

a membrane. The derivation assumes that the interfaces are parallel and planar. We present the 3D relation relevant to a membrane in space and the 2D relation relevant within a single planar section.

We assume that, over the spatial scale sampled by a probe line, the two bounding surfaces of the barrier are separated by a constant perpendicular distance h. Let Θ be the incidence angle between the probe direction and the normal of the planar interfaces such that $0 \leq \Theta \leq \pi/2$. Elementary geometry gives the relationship between the thickness h and the measured intercept length T along the probe as

$$\frac{1}{T} = \frac{\cos\Theta}{h}. \tag{B.1}$$

This is where the assumption of parallel and planar surfaces/perimeters enters. The probability $g(\Theta)$ that a randomly oriented line will make an angle Θ with the interfaces is proportional to $\sin\Theta$ in three dimensions, but is uniformly weighted in two dimensions. However, the probability $h(\text{hit}|\Theta)$ that the line will make any intersection at all given Θ, is proportional to $\cos\Theta$ in both cases.

Considering only lines which hit the interfaces, from Bayes's theorem the distribution f of Θ, given an intersection, is proportional to the product of these distributions

$$f(\Theta|\text{hit}) \propto g(\Theta)h(\text{hit}|\Theta). \tag{B.2}$$

Therefore, the probability distribution for Θ is given by the normalised probability density functions

$$f_{2D}(\Theta|\text{hit}) = \cos\Theta \tag{B.3}$$

for two dimensions, and

$$f_{3D}(\Theta|\text{hit}) = 2\cos\Theta\sin\Theta \tag{B.4}$$

for three dimensions.

By substituting (B.1) into (B.3) and (B.4) we obtain (showing 3D calcu-

lation outside of brackets and corresponding 2D calculation in brackets)

$$\begin{aligned}
\mathbb{E}\left[\frac{1}{T}\right] &= \int_0^{\pi/2} \frac{\cos\Theta}{h}\, f_{3D}(\Theta|\text{hit})\, d\Theta \quad \left(\int_0^{\pi/2} \frac{\cos\Theta}{h}\, f_{2D}(\Theta|\text{hit})\, d\Theta\right) \\
&= \frac{1}{h}\int_0^{\pi/2} 2\cos^2\Theta\, \sin\Theta\, d\Theta \quad \left(\frac{1}{h}\int_0^{\pi/2} \cos^2\Theta\, d\Theta\right) \\
&= \frac{2}{3h} \quad \left(\frac{\pi}{4h}\right),
\end{aligned} \tag{B.5}$$

and thus

$$h = \frac{2}{3}\, T_h \quad \left(\frac{\pi}{4}\, T_h\right). \tag{B.6}$$

where T_h is the harmonic mean of random intercept lengths. This is an exact relation under the assumption of parallel, planar surfaces/perimeters but is only an approximation otherwise.

Appendix C. Methodology for simulated stereological experiments

This appendix describes the full 2D workflow used to estimate, via stereology methods, the tissue–IVS and tissue–capillary perimeters in each slice and the harmonic-mean exchange-barrier thickness, together with bootstrap confidence intervals.

Appendix C.1. Method for obtaining random sliced geometries

In COMSOL, a rectangular bounding box is drawn around each villus. This is necessary as stereological methods for calculating surface area find surface area density and so a fixed volume must be imposed to calculate surface areas. Random 2D sliced geometries are sampled by a well-known method (Muller, 1959). First, three independent standard normal variables are sampled

$$[\hat{\mathbf{e}}_x, \hat{\mathbf{e}}_y, \hat{\mathbf{e}}_z] \sim [\mathcal{N}(0,1), \mathcal{N}(0,1), \mathcal{N}(0,1)], \tag{C.1}$$

where $\mathcal{N}(0,1)$ denotes the standard normal distribution. Then, a unit normal vector is formed by normalising this sample,

$$\mathbf{n} = \frac{[\hat{\mathbf{e}}_x, \hat{\mathbf{e}}_y, \hat{\mathbf{e}}_z]}{|[\hat{\mathbf{e}}_x, \hat{\mathbf{e}}_y, \hat{\mathbf{e}}_z]|}. \tag{C.2}$$

Next, a uniformly-random plane orthogonal to $\mathbf{n}$ is sampled from the set of all such planes that intersect the bounding box.

The resulting 2D geometries contain up to three families of curves: the curves that define the bounding box projected onto the plane; the curves which define the tissue surface; and the curves which define the vessel surfaces. In COMSOL a calculation of $\mathcal{L}_p$ was made on each slice by first solving the 2D Laplace equation between the tissue and vessel perimeters and then integrating the result along the tissue perimeter according to (A.3). The total perimeter length of the tissue P_t and vessels P_v were calculated using COMSOL's measurement tools.

Appendix C.2. Input data and physical scaling

The sliced 2D images were exported as 3000×1500 pixel jpegs, along with a measurement which defines the physical length represented by each side of each square pixel. The segmentation algorithm produces a label image LAB with four classes:

- 0: outside the region of interest (ROI)
- 1: tissue
- 2: capillary
- 3: intervillous space (IVS)

Only pixels with labels in $\{1, 2, 3\}$ are inside the ROI.

Appendix C.3. Segmentation algorithm

The algorithm consists of two stages: detection of the edges of the ROI and classification of pixels within the ROI into tissue, capillary, and IVS.

Detection of the ROI polygon (projection of inner box to the slice plane)

1. The RGB image is converted to grayscale.
2. The black features in the image (the axes and the bounding box) are identified using an automatic thresholding step that picks out dark pixels.
3. After identifying non-dark pixels, MATLAB's `imclearborder` function is applied, which deletes any connected non-dark region that reaches the outer edge of the image. The remaining non-dark region is therefore the enclosed interior of the ROI, surrounded by the dark frame.

4. The polygonal border of the ROI is detected using MATLAB's `bwboundaries` function and stored as a closed polygon with K vertices by listing the pixel coordinates $\{(x_k, y_k)\}_{k=1}^{K}$ around its edge.
5. The ROI area is computed directly from the label image as

$$A_{\mathrm{ROI}} \;=\; N_{\mathrm{ROI}}\, L^2, \tag{C.3}$$

   where N_{ROI} is the number of pixels within the ROI polygon.

Classification within the ROI into tissue, capillary, and IVS

1. The RGB image is lightly denoised using MATLAB's bilateral filter (`imbilatfilt`), applied separately to each colour channel to reduce pixel-level noise while preserving sharp boundaries.
2. The image is transformed into CIELab colour space, providing the lightness channel L^* and chromaticity channels a^* (green–red) and b^* (blue–yellow).
3. To distinguish IVS (bright regions) from tissue and vessels (darker regions), we compute an automatic threshold on the L^* values within the ROI using MATLAB's `graythresh` function. Pixels with L^* below this threshold are labelled as non-white.
4. Vessels are identified inside this object mask by k-means clustering in the (a^*, b^*) plane. The vessel cluster is selected as the one with lower mean b^* (more blue).
5. Tissue is defined as the object mask excluding capillaries, and IVS is defined as ROI pixels not assigned to tissue or capillary.
6. Labels are assigned as IVS $\to$ 3, tissue $\to$ 1, capillary $\to$ 2, and outside ROI $\to$ 0.
7. Overlays of the segmented boundary on top of the original images are inspected for quality. A small amount of post-processing is applied by eroding the capillary mask by 1-2 pixels to visually give a clearer fit.
8. A final smoothing step is applied to reduce jagged label boundaries.

Appendix C.4. Random-line generation

Random test lines are generated so that their orientations are isotropic and their placements are uniform with respect to translation over the ROI. For each random line

1. Sample an orientation angle
$$\theta \sim \mathrm{Unif}[0, \pi).$$
Define the unit normal and unit direction vectors
$$\mathbf{n}(\theta) = (\cos\theta,\ \sin\theta), \qquad \mathbf{u}(\theta) = (-\sin\theta,\ \cos\theta).$$
2. To determine the range of line positions that intersect the ROI, each polygon vertex is projected onto $\mathbf{n}(\theta)$ and the minimum and maximum values across all vertices is taken
$$s_{\min}(\theta) = \min_{k=1,\dots,K} \big(\mathbf{n}(\theta)\cdot(x_k, y_k)\big), \qquad s_{\max}(\theta) = \max_{k=1,\dots,K} \big(\mathbf{n}(\theta)\cdot(x_k, y_k)\big).$$
3. Sample an offset (signed distance) uniformly from this interval:
$$s \sim \mathrm{Unif}\big[s_{\min}(\theta),\ s_{\max}(\theta)\big].$$
4. The infinite line is defined implicitly by
$$\mathbf{n}(\theta) \cdot (x, y) = s.$$
5. Intersect this infinite line with the ROI polygon to yield a line segment within the ROI.

This procedure produces isotropic orientations and a uniform distribution of line offsets for each θ, which is the standard construction for IUR lines within a bounded domain.

Appendix C.5. Test system: isotropic uniform random lines and discretisation

For each slice, N_{lines} isotropic uniform random (IUR) test lines are generated, and the portion of the line lying within the ROI is traversed at a fixed step size of 0.25 pixels. This yields:

- the in-ROI test length for each line in μm,
- a one-dimensional sequence of labels along the line at uniform arclength increments,
- label transitions used to count interface intercepts,
- tissue chord lengths used for thickness estimation.

The total test-line length in the slice is
$$L_T = \sum_{j=1}^{N_{\text{lines}}} \ell_j. \tag{C.4}$$

Appendix C.6. Perimeter estimation from intercept counts

Two interfaces are considered:

- tissue–IVS interface (labels 1 and 3), with intercept count I_{31},
- tissue–capillary interface (labels 1 and 2), with intercept count I_{12}.

An intercept is counted whenever adjacent samples along a test line cross the relevant interface (both directions are counted equally). Per-slice estimates of tissue–IVS perimeter and tissue–vessel perimeter respectively are obtained by multiplying by the ROI area

$$\widehat{P}_t \;=\; A_{\mathrm{ROI}}\,\frac{\pi}{2}\,\frac{I_{31}}{L_T}, \qquad \widehat{P}_v \;=\; A_{\mathrm{ROI}}\,\frac{\pi}{2}\,\frac{I_{12}}{L_T}. \tag{C.5}$$

Appendix C.7. Thickness estimation from lineal intercepts

Thickness is estimated from tissue chords extracted along the sampled IUR lines. Each tissue chord is defined as a contiguous run of label 1 (tissue) along a line that is flanked by IVS and capillary (in either order) along that line, corresponding to a local sequence 3−1−2 or 2−1−3. The physical chord lengths $\{t_k\}$ are computed from the number of steps in the run, the step size (0.25 pixels), and the pixel scale L.

The harmonic mean of the chord lengths is

$$H(\{t_k\}) \;=\; \left(\frac{1}{n}\sum_{k=1}^{n}\frac{1}{t_k}\right)^{-1}. \tag{C.6}$$

The slice-level harmonic-mean thickness estimate is then

$$\widehat{h} \;=\; \frac{\pi}{4}\,H(\{t_k\}). \tag{C.7}$$

Appendix C.8. Slice-level estimate of the diffusive length proxy

For each slice we compute diffusive length-scale per unit depth

$$\widehat{\mathcal{L}}_p \;=\; \frac{\widehat{P}_t + \widehat{P}_v}{2\,\widehat{h}}, \tag{C.8}$$

and physics-based thickness

$$h \;=\; \frac{P_t + P_v}{2\,\mathcal{L}_p}. \tag{C.9}$$

Appendix C.9. Bootstrap confidence intervals by resampling lines

Sampling uncertainty arising from the finite number of random test lines is quantified using a nonparametric bootstrap performed at the level of test lines for each slice.

For each slice, the implementation stores per-line quantities:

- $I_{31,j}$: tissue–IVS intercepts contributed by line j,
- $I_{12,j}$: tissue–capillary intercepts contributed by line j,
- ℓ_j: in-ROI test length for line j,
- $\{t_k\}_j$: the set of tissue chord lengths contributed by line j.

A bootstrap replicate is formed by resampling the N_{lines} lines with replacement. For replicate b, totals are computed as

$$I_{31}^{(b)} = \sum_{j \in \mathcal{S}_b} I_{31,j}, \quad I_{12}^{(b)} = \sum_{j \in \mathcal{S}_b} I_{12,j}, \quad L_T^{(b)} = \sum_{j \in \mathcal{S}_b} \ell_j, \tag{C.10}$$

and the perimeter estimates $\widehat{P}_t^{(b)}$, $\widehat{P}_v^{(b)}$ are obtained using the formulae above. The thickness estimate $\widehat{h}^{(b)}$ is obtained by pooling the chord lengths contributed by the resampled lines and applying the estimator above. The length proxy is then computed as

$$\widehat{\mathcal{L}}_p^{(b)} \;=\; \frac{\widehat{P}_t^{(b)} + \widehat{P}_v^{(b)}}{2\,\widehat{h}^{(b)}}. \tag{C.11}$$

Confidence intervals are obtained from the empirical bootstrap distributions. A nominal 95% confidence interval is taken as the 2.5th and 97.5th percentiles.

Appendix C.10. Benchmark experiments on simplified geometries

To help interpret the stereological errors observed on realistic villus slices, we also performed two benchmark experiments on simplified synthetic geometries. In each case we construct a labelled 2D image with a known barrier thickness, apply the same stereological thickness estimator as used in the main experiments, and compute their relative error. These simplified tests allow us to isolate two expected sources of bias: finite aspect ratio, and curvature.

Finite-aspect-ratio barrier (planar band)

We first consider a horizontal planar barrier of constant thickness spanning the full image width. This geometry isolates the effect of barrier aspect ratio. A square field of view of physical side-length

$$L_{\text{phys}} = 3000\ \mu\text{m} \tag{C.12}$$

is discretised into a $N \times N$ pixel image. The pixel size is therefore

$$\Delta x = L_{\text{phys}}/N. \tag{C.13}$$

For each trial and each tested thickness, we construct a horizontal band centered in the image that represents a tissue barrier between IVS and vessel regions. The pixels are labelled following the scheme in Appendix C.3.

A range of thicknesses d of the barrier are tested, and the corresponding aspect ratio is defined as

$$\mathrm{A}_R = d/L_{\text{phys}}. \tag{C.14}$$

To limit any error due to pixellation effects, the image resolution N is adjusted with thickness so that the barrier remains similarly well-resolved for different aspect ratios

$$N \approx N_0 \frac{d_{\max}}{d}, \tag{C.15}$$

where N_0 is a fixed resolution parameter and $d_{\max}$ is the largest tested thickness.

For each synthetic image, the stereological harmonic-mean thickness estimator is applied using N_{lines} random lines as described in Appendix C.7. For each barrier thickness, the relative error reported between the exact thickness and the estimated thickness in Figure 3(a,c) is

$$\varepsilon_{\mathrm{A}_R} = \frac{d - \widehat{h}}{d}. \tag{C.16}$$

The experiment is repeated over many independent trials in order to estimate the mean bias as a function of aspect ratio and to visualise the scatter due to random-line placement.

Curvature bias (concentric circular interfaces)

To isolate curvature effects, we next consider a barrier between two concentric circles with fixed thickness but varying radius. In this case the barrier is locally curved, with curvature set by the outer radius.

A square field of view of the same physical side-length $L_{\text{phys}} = 3000\ \mu\text{m}$ is discretised. For each geometry we specify an outer diameter D_{outer} and an inner diameter

$$D_{\text{inner}} = D_{\text{outer}} - 200\ \mu\text{m}, \tag{C.17}$$

so that the actual barrier thickness is constant across all cases:

$$d = \frac{D_{\text{outer}} - D_{\text{inner}}}{2} = 100\ \mu\text{m}. \tag{C.18}$$

We test several outer diameters so that the curvature increases as the outer diameter decreases. This setup represents IVS outside both circles, tissue in the annular region and vessel inside the smaller circle, and the pixels are once again labelled according to the scheme from Appendix C.3.

For each annulus, the same stereological harmonic-mean thickness estimate $\widehat{h}$ is computed using random lines as in Appendix C.7. To express curvature effects in a dimensionless form, results are plotted against $d\kappa$, where κ is the curvature of the circular interface. Since $\kappa = 1/R$ for a circle of radius $R = D_{\text{outer}}/2$, we compute

$$d\kappa = \frac{2d}{D_{\text{outer}}}. \tag{C.19}$$

The reported relative error is

$$\varepsilon_{d\kappa} = \frac{d - \widehat{h}}{d}. \tag{C.20}$$

We repeat the experiment over many independent trials and compute the mean error as a function of $d\kappa$. A best-fit line constrained to pass through the origin is also plotted to summarise the approximately linear dependence of error on $d\kappa$ (Fig. 3b,d).

These two benchmark experiments provide controlled reference cases for interpreting thickness-estimation bias: the planar band isolates finite-aspect-ratio effects, while the annulus isolates curvature-driven deviations from the locally-flat assumption implicit in the stereological correction factors.

Appendix C.11. Quantification of error due to pixellation

The benchmark experiments in Appendix C.10 are performed on synthetic label images and therefore introduce an additional numerical error associated with discretising a smooth geometry on a pixel grid. To quantify the magnitude of this pixellation error, we considered a single planar-band

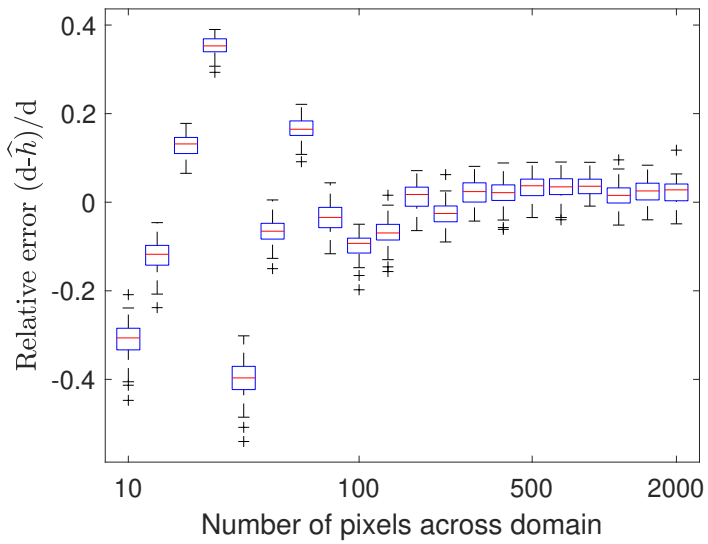

Figure C.1: Convergence of stereological thickness estimation with image resolution for a planar-band barrier of fixed aspect ratio 0.0667. For each number of pixels across the square domain, the harmonic-mean thickness estimator was applied using 200 isotropic uniform random test lines, repeated over 100 independent trials. Boxplots show the distribution of relative error $(d - \widehat{h})/d$ at each resolution converging towards a constant.

barrier of fixed aspect ratio 0.0667, and repeated the stereological thickness estimation while systematically increasing the image resolution.

For a series of resolutions (number of pixels across the square domain), we generated 100 independent realisations of the random-line sampling procedure using 200 isotropic uniform random test lines per trial. For each trial we computed the relative thickness error

$$\frac{d - \widehat{h}}{d}, \tag{C.21}$$

where d is the true barrier thickness and $\widehat{h}$ is the stereological harmonic-mean thickness estimate (Eq. C.6). Figure C.1 summarises the distribution of the relative error at each resolution using boxplots, demonstrating convergence of the estimator as number of pixels increases. This analysis confirms that, above a sufficiently fine resolution, the remaining bias in the planar-band experiment is not sensitive to pixellation.

Appendix D. Relationship between $\mathcal{L}$, surface area divided by thickness and curvature

If we have an annular region in 3D (2D) between two concentric spheres (circles) with radii $R_1 > R_2$, the solution to Laplace's equation for dependent variable c in the annular region according to $c = 1$ on the outer surface (perimeter) and $c = 0$ on the inner surface (perimeter) is given by the well-known solution

$$c = \frac{R_1(r - R_2)}{r(R_1 - R_2)} \qquad \left(\frac{\ln(r/R_2)}{\ln R_1/R_2}\right). \tag{D.1}$$

Taking the radial component of the gradient of c and integrating it around the outer surface (perimeter) gives us

$$\mathcal{L} = \frac{4\pi R_1 R_2}{R_1 - R_2} \qquad \left(\mathcal{L}_p = -\frac{2\pi}{\ln R_2/R_1}\right). \tag{D.2}$$

Calling $d = R_1 - R_2$, and assuming $d \ll R_1$ so that $\ln(R_2/R_1) = -d/R_1 - d^2/2R_1^2 + \ldots$ we get

$$\mathcal{L} = \frac{4\pi R_1^2}{d}(1 - d\kappa_1) \qquad \left(\mathcal{L}_p = \frac{2\pi R_1}{d}\left(1 - \frac{d\kappa_1}{2}\right)\right), \tag{D.3}$$

where $\kappa_1 = 1/R_1$. This shows that surface area (perimeter) divided by thickness overestimates $\mathcal{L}$ ($\mathcal{L}_p$).

References

Baergen, R.N., Burton, G.J., Kaplan, C.G., 2022. Benirschke's Pathology of the Human Placenta. 7th ed., Springer Nature.

Bappoo, N., Tongpob, Y., Hakim, M., Myers, J., Panting, E., Chapman, K.E., Thomson, A.J., Moran, C.M., Kelsey, L.J., Srinivasan, V., James, J.L., Clark, A.R., Doyle, B.J., Wyrwoll, C.S., 2024. Feto-placental vascular structure and in silico haemodynamics: Of mice, rats, and human. Placenta 158, 175–184.

Barapatre, N., Halm, L., Schmitz, C., von Koch, F., Kampfer, C., Frank, H.G., 2026. Structural alterations in the placental villous tree in well-controlled gestational diabetes mellitus. Placenta 175, 25–32.

Chappell, J., Aughwane, R., Clark, A.R., Ourselin, S., David, A.L., Melbourne, A., 2023. A review of feto-placental vasculature flow modelling. Placenta 142, 56–63.

COMSOL AB, 2024. COMSOL Multiphysics® v. 6.3. Stockholm, Sweden. URL: https://www.comsol.com.

Cruz-Orive, L.M., 2017. Stereology: a historical survey. Image Anal. Stereol. 36, 153–177.

Erlich, A., Pearce, P., Mayo, R.P., Jensen, O.E., Chernyavsky, I.L., 2019. Physical and geometric determinants of transport in fetoplacental microvascular networks. Sci. Adv. 5, eaav6326.

Feneley, M.R., Burton, G.J., 1991. Villous composition and membrane thickness in the human placenta at term: a stereological study using unbiased estimators and optimal fixation techniques. Placenta 12, 131–142.

Gill, J.S., Salafia, C.M., Grebenkov, D., Vvedensky, D.D., 2011. Modeling oxygen transport in human placental terminal villi. J. Theor Biol. 291, 33–41.

Gundersen, H.J.G., Jensen, T.B., Østerby, R., 1978. Distribution of membrane thickness determined by lineal analysis. J. Microscopy 113, 27–43.

Jackson, M.R., Joy, C.F., Mayhew, T.M., Haas, J.D., 1985. Stereological studies on the true thickness of the villous membrane in human term placentae: a study of placentae from high-altitude pregnancies. Placenta 6, 249–258.

Jensen, E.B., Gundersen, H.J.G., Østerby, R., 1979. Determination of membrane thickness distribution from orthogonal intercepts. J. Microscopy 115, 19–33.

Jensen, O.E., Chernyavsky, I.L., 2019. Blood flow and transport in the human placenta. Annu. Rev. Fluid Mech. 51, 25–47.

Lewis, R.M., Pearson-Farr, J.E., 2020. Multiscale three-dimensional imaging of the placenta. Placenta 102, 55–60.

Mayhew, T.M., 2006. Stereology and the placenta: where's the point? – A review. Placenta 27, 17–25.

Mayhew, T.M., Joy, C.F., Haas, J.D., 1984. Structure-function correlation in the human placenta: the morphometric diffusing capacity for oxygen at full term. J. Anat. 139, 691–708.

Mayhew, T.M., Manwani, R., Ohadike, C., Wijesekara, J., Baker, P.N., 2007. The placenta in pre-eclampsia and intrauterine growth restriction: studies on exchange surface areas, diffusion distances and villous membrane diffusive conductances. Placenta 28, 233–238.

Muller, M.E., 1959. A note on a method for generating points uniformly on n-dimensional spheres. Comm. ACM 2, 19–20.

Nye, G.A., Ingram, E., Johnstone, E.D., Jensen, O.E., Schneider, H., Lewis, R.M., Chernyavsky, I.L., Brownbill, P., 2018. Human placental oxygenation in late gestation: experimental and theoretical approaches. J. Physiol. 596, 5523–5534.

Ong, P.J.L., Burton, G.J., 1991. Thinning of the placental villous membrane during maintenance in hypoxic organ culture: structural adaptation or syncytial degeneration? Eur. J. Obstet. Gynecol. Reprod. Biol. 39, 103–110.

Perazzolo, S., Lewis, R.M., Sengers, B.G., 2017. Modelling the effect of intervillous flow on solute transfer based on 3D imaging of the human placental microstructure. Placenta 60, 21–27.

Plitman Mayo, R., Abbas, Y., Charnock-Jones, D.S., Burton, G.J., Marom, G., 2019. Three-dimensional morphological analysis of placental terminal villi. Interface Focus 9, 20190037.

Plitman Mayo, R., Charnock-Jones, D.S., Burton, G.J., Oyen, M.L., 2016. Three-dimensional modeling of human placental terminal villi. Placenta 43, 54–60.

Romppanen, T., Collan, Y., 1983. Practical guidelines for a morphometric study. Acta Stereol. 2, 274–297.

Sun, C., Groom, K.M., Oyston, C., Chamley, L.W., Clark, A.R., James, J.L., 2020. The placenta in fetal growth restriction: What is going wrong? Placenta 96, 10–18.

Tun, W.M., Poologasundarampillai, G., Bischof, H., Nye, G., King, O.N.F., Basham, M., Tokudome, Y., Lewis, R.M., Johnstone, E.D., Brownbill, P., Darrow, M., Chernyavsky, I.L., 2021. A massively multi-scale approach to characterizing tissue architecture by synchrotron micro-CT applied to the human placenta. J. R. Soc. Interface 18, 20210140.

Weibel, E.R., Knight, B.W., 1964. A morphometric study on the thickness of the pulmonary air-blood barrier. J. Cell Biol. 21, 367–384.

Yong, H.E.J., Maksym, K., Yusoff, M.A.B., Salazar-Petres, E., Nazarenko, T., Zaikin, A., David, A.L., Hillman, S.L., Sferruzzi-Perri, A.N., 2023. Integrated placental modelling of histology with gene expression to identify functional impact on fetal growth. Cells 12, 1093.